

Phys Chem C Nanomater Interfaces, Author manuscript; available in PMC 2010 August 6.

Published in final edited form as:

J Phys Chem C Nanomater Interfaces. 2009 August 6; 113(31): 13593-13599. doi:10.1021/jp902953t.

# A Facile Hydrothermal Synthesis of Iron Oxide Nanoparticles with Tunable Magnetic Properties

Song  $Ge^{1,2}$ , Xiangyang  $Shi^{3,*}$ , Kai  $Sun^4$ , Changpeng  $Li^1$ , James R. Baker  $Jr.^2$ , Mark M. Banaszak  $Holl^{2,5}$ , and Bradford G.  $Orr^{1,2,*}$ 

- <sup>1</sup> Department of Physics, University of Michigan, Ann Arbor, Michigan 48109, USA
- <sup>2</sup> Michigan Nanotechnology Institute for Medicine and Biological Sciences, University of Michigan, Ann Arbor, Michigan 48109, USA
- <sup>3</sup> College of Chemistry, Chemical Engineering, and Biotechnology, Donghua University, Shanghai 201602, P. R. China
- <sup>4</sup> Department of Materials Science and Engineering, University of Michigan, Ann Arbor, Michigan 48109, USA
- <sup>5</sup> Department of Chemistry, University of Michigan, Ann Arbor, Michigan 48109, USA

## **Abstract**

We report a facile one-step hydrothermal approach to the synthesis of iron oxide (Fe<sub>3</sub>O<sub>4</sub>) nanoparticles (NPs) with controllable diameters, narrow size distribution, and tunable magnetic properties. In this approach, the iron oxide NPs were fabricated by oxidation of FeCl<sub>2</sub>·4H<sub>2</sub>O in basic aqueous solution under an elevated temperature and pressure. Transmission electron microscopy (TEM) and X-ray diffraction (XRD) studies reveal that the particles are highly crystalline and that the diameters of the particles can be tuned from 15 nm to 31 nm through the variation of the reaction conditions. The NPs exhibit high saturation magnetization in the range of  $53.3 \sim 97.4$  emu/g and their magnetic behavior can be either ferromagnetic or superparamagnetic depending on the particle size. A superconducting quantum interference device magnetorelaxometry (SQUID-MRX) study shows that the size of the NPs significantly affects the detection sensitivity. The investigated iron oxide NPs may find many potential biological applications in cancer diagnosis and treatment.

#### **Keywords**

Hydrothermal synthesis; iron oxide nanoparticles; magnetic properties; and SQUID magnetorelaxometry

## Introduction

The synthesis of various functional nanomaterials such as metals, semiconductors, and magnetic materials etc. has been of immense scientific and technological interest. 1<sup>-3</sup> Among these nanomaterials, magnetic nanoparticles (NPs) have been extensively studied and applied in numerous fields, such as magnetic recording media, sensors, spintronics and many biological applications including cell type recognition, drug delivery, targeted therapeutics, and intracellular imaging. 4-8 Magnetite (Fe<sub>3</sub>O<sub>4</sub>) NPs are a common magnetic material with a cubic inverse spinel structure that have been extensively investigated and used as an *in vivo* contrast

<sup>\*</sup>To whom correspondence should be addressed. xshi@dhu.edu.cn (X. Shi), orr@umich.edu (B. G. Orr).

agent for cancer diagnosis.  $^{9-12}$  The applications for the Fe<sub>3</sub>O<sub>4</sub> NPs often require a controllable synthesis to obtain particles with desirable size and tunable magnetic properties. This remains a great challenge.

Magnetite NPs are commonly synthesized through a controlled co-precipitation of Fe (II) and Fe (III) ions in a basic aqueous solution.  $^{13}$ –16 This method generates Fe<sub>3</sub>O<sub>4</sub> NPs with a diameter around 10 nm, hence lacking the ability to control the particle size. Organic phase synthesis of iron oxide NPs has been recently developed. Though the Fe<sub>3</sub>O<sub>4</sub> NPs display a narrow size distribution and the synthetic procedure allows fine control of the particle size from several nanometers up to about 20 nm,  $^{17,18}$  the approach involves toxic organic reagents and a high reaction temperature. Moreover, phase transfer of the NPs to aqueous solution is necessary when these particles are used for biological applications.  $^{19,20}$  These difficulties suggest that development of new approaches to synthesizing size- and property-tunable magnetic NPs soluble in aqueous solution is important for their further biological applications.

To evaluate and detect the magnetic NPs, a superconducting quantum interference device (SQUID) is one of the best tools due to the fact that it is the most sensitive detector of magnetic field. The use of SQUID in the biological environment to detect the minute amount of magnetic NPs in the human body was first attempted by Cohen to examine the damage of human lungs by minerals. More recently, advances in biological nanotechnology have shown that the surface of NPs can be modified with specific ligands for subsequent targeting the particular tissues through ligand-receptor interaction. 11,12,22–25,19 Because of the high sensitivity and non-invasive nature, SQUID imaging appears as a promising technology for diagnosing a tissue that specifically uptakes the targeted magnetic NPs.

So far, three SQUID methods have been used for detecting the magnetic NPs: remanence,26·27 susceptibility,28<sup>-30</sup> and magnetorelaxometry (MRX),<sup>31-35</sup> where MRX records the magnetic relaxation process. In general, the relaxation time of magnetic NPs is mainly dependent on their size. Therefore, the size and size distribution are key factors in determining the sensitivity of MRX. Unfortunately, in most previously reported MRX results, commercialized NPs were used and it has been difficult to synthesize size-tunable, water-soluble magnetic NPs to achieve the optimal MRX sensitivity.34·36

In this present work, a simple, facile hydrothermal approach was developed to synthesize  $Fe_3O_4$  NPs. We show that the size of the formed  $Fe_3O_4$  NPs can be tuned through variation of the reaction conditions. Accordingly the magnetic properties of the synthesized  $Fe_3O_4$  NPs can be varied. These NPs were investigated using a superconducting quantum interference device magnetorelaxometry (SQUID-MRX) technique and the results clearly reveal that the particle size can significantly affect the MRX sensitivity. The developed synthetic approach allows fine control of the particle sizes and hence the magnetic properties of the formed  $Fe_3O_4$  NPs, thus providing a unique platform for their biomedical applications.

# **Experimental section**

#### **Materials**

All chemicals used were reagent grade from commercial sources. FeCl<sub>2</sub>·4H<sub>2</sub>O (99%) and ammonia (28%) were purchased from Aldrich. Ethanol was obtained from AAPER Alcohol & Chemistry Co. Water used in all experiments was purified using a Milli-Q Plus 185 water purification system (Millipore, Bedford, MA) with resistivity higher than 18  $M\Omega$ ·cm.

## Synthesis of Fe<sub>3</sub>O<sub>4</sub> NPs

In a typical synthesis (e.g., Product 1 in Table 1), FeCl<sub>2</sub>·4H<sub>2</sub>O (0.5 g) was dissolved in 25 mL water. Under vigorous stirring, ammonium hydroxide (2.5 mL) was added and the suspension

was continuously stirred in air for 10 min, allowing the iron (II) to be oxidized. The reaction mixture was then autoclaved (Tuttnauer 2540M Analog Autoclave, Krackeler Scientific, Inc, Albany, NY) in a sealed pressure vessel with a volume of 48 mL at 134°C for 3 h under air with a gauge pressure of 2 bar and cooled down to room temperature. The black precipitate was collected and purified with water via a centrifugation-dispersion process. The final  $Fe_3O_4$  NP suspension was lyophilized to obtain black dry powder.

## Transmission electron microscopy (TEM)

TEM experiments were performed either on a Philips CM-100 microscope operating at 60 kV or on a JEOl 2010F analytical electron microscope operating at 200 kV. The former TEM was equipped with a Hamamatsu digital Camera ORCA-HR and operated using AMT software (Advanced Microscopy Techniques Corp, Danver, MA) for the study of the NP morphology. The latter TEM was used to analyze the selected area electron diffraction (SAED) of the NPs. TEM samples were prepared by placing one drop of diluted iron oxide suspension (5  $\mu$ L) onto a 200-mesh carbon-coated copper grids and air-dried before measurements.

# X-ray diffraction (XRD)

The crystalline structure and the size of the products were determined by a Scintag powder XRD system using Cu K $\alpha$  radiation with a wavelength of 1.5404 Å at 40 kV and 30 mA. First, a coarse scan from 20° to 70° (20) was performed to acquire an overall spectrum to identify the crystal structure. Then, a finer scan of the major peak was repeated to produce a smoother peak for better estimating the size of NPs.

# X-ray photoelectron spectroscopy (XPS)

XPS was performed using a Kratos Ultra DLD XPS operated at 15 kV using a monochromated Al source that can give an energy resolution of  $\sim 0.5$  eV. Both broad and narrow (or core) scans were carried out to collect XPS spectra.

#### Superconducting quantum interference device (SQUID) magnetometry

The magnetic hysteresis loops were measured using a Quantum Design MPMS-5 SQUID magnetometer (San Diego, CA) at room temperature. The Fe<sub>3</sub>O<sub>4</sub> NP powder was loaded into a plastic capsule and the capsule was put into a plastic straw before measurement.

# SQUID magnetorelaxometry (SQUID-MRX)

Experimental control—A different SQUID system based on magnetorelaxometry was built in our lab and used to test the synthesized Fe<sub>3</sub>O<sub>4</sub> NPs for medical imaging applications. The SQUID is a 2nd order gradiometer system (Model 601 DC LTS) provided by Tristan Technology Inc. The measurement was performed in two screen rooms: an rf-screen room and a mu-metal shield. The former can significantly reduce the noise above kilohertz and the latter was mainly used to minimize the 60 Hz noise and magnetic influence. The sample was placed at a distance of 1.5 cm to the SQUID sensor. A typical measurement sequence was designed as follows: (1) apply a reset pulse to the SQUID feedback controls; (2) apply current to the excitation coil to produce magnetizing field of ~15 G for 1 s; (3) turn off the current quickly (within several ms); and (4) after 20 ms delay, remove the reset pulse and start data acquisition for 1 s. This sequence was repeated 10 times and averaged for each sample to enhance the signal to noise ratio. The unavoidable background signal was subtracted. To prepare a sample for SQUID-MRX measurement, a known amount of Fe<sub>3</sub>O<sub>4</sub> NPs was suspended in deionized water (with a pH value of 6.0) and vortexed to achieve good dispersion. Serial dilutions were prepared and each was loaded onto a piece of filter paper with the area of  $\sim 0.5 \times 0.5$  cm<sup>2</sup>. The loaded filter paper was air dried before SQUID-MRX measurements.

**Theoretical model**—The magnetic relaxation of NPs after magnetization takes place via two different mechanisms: Brownian relaxation and Nèel relaxation. Brownian relaxation is induced by the physical rotation of the particles in the carrier solution with time constant

$$\tau_{\rm B} = 3V' \eta / k_{\rm B} T \tag{1}$$

where V' is the hydrodynamic volume of the particle and  $\eta$  the dynamic viscosity. Nèel relaxation is due to the reorientation of the magnetization vectors inside the particles, the time constant of which is expressed by

$$\tau_N = \tau_0 \exp(-KV/k_B T) \tag{2}$$

where  $\tau_0$  is usually quoted as  $10^{-9}$  s, K is the anisotropy constant in the range of  $(1-5)\times 10^4$  J/m<sup>3</sup>.<sup>37,38</sup> When the NPs are immobilized, the relaxation can only happen through the Nèel mechanism which is very sensitive to the particle size. The magnetic signal decay, instead of being exponential, takes a logarithmic form due to the size distribution of the magnetic NPs. In terms of the detected field by SQUID, the decay can be expressed as

$$B(t) = B_0 \ln(1 + t_c/t) + B' \tag{3}$$

where the characteristic time  $t_c = t_{mag}$  (time of biasing field applied) in case of weak magnetization field.  $^{39}$  B' means an arbitrary static field, which has no physical significance since SQUID only measures change in fields.  $B_0$  reflects the amplitude of the decay, which depends on the amount, size distribution of particles, and temperature. So for a particular sample of NPs at a certain temperature,  $B_0$  is directly related to the amount of NPs. In our experiments, the data were fitted and the relationship between the best fitting parameter  $B_0$  and the amount of NPs was established.

## Results and discussion

#### Characterization of Fe<sub>3</sub>O<sub>4</sub> NPs

A typical TEM image of the as-synthesized  $Fe_3O_4$  NPs (Product 1 listed in Table 1) is shown in Figure 1a. In the image, the NPs exhibit spherical or slightly ellipsoidal shape. Statistical analysis of the size of the particles (Figure 1b) shows that the average diameter of the NPs is  $31.1 \pm 6.1$  nm, indicating that the NPs are uniform when compared with other  $Fe_3O_4$  NPs synthesized in aqueous conditions.11 $\cdot$ 40 $\cdot$ 41 The selected area electron diffraction (SAED) pattern of the same  $Fe_3O_4$  NPs (Figure 1c) confirmed a typical magnetite crystalline structure. 42,43

The composition of these nanocrystals was identified by XPS (Figure 2). The survey scan shows clear peaks corresponding to the binding energies of  $Fe_{2p}$  and  $O_{1s}$  (Figure 2a). Further fine scanning around the  $Fe_{2p}$  peaks reveals two characteristic binding energy peaks at 710.4 and 723.3 eV for  $Fe_{2p3/2}$  and  $Fe_{2p1/2}$ , respectively, which are consistent with the reported values of  $Fe_3O_4$  in literature (Figure 2b).<sup>44,45</sup> Other peaks in the spectrum (Figure 2a) are ascribed to the indium substrate and carbon contamination on the substrate.

## Size-control of the Fe<sub>3</sub>O<sub>4</sub> NPs

After the  $Fe_3O_4$  NPs with a diameter of 31 nm were synthesized and characterized, we expected that by altering the reaction conditions, the size of  $Fe_3O_4$  NPs could be controlled. To test the influence of  $FeCl_2$  concentration on the size of the as-synthesized NPs, our experiments were designed to minimize the change of other parameters. First, we kept a constant volume of the mixture solution (14 mL) in the pressure glass vessel to ensure that a similar amount of oxygen was used for the oxidation of Fe (II). And the volume of ammonium was adjusted proportional to the amount of  $FeCl_2$ . A series of changes on the experimental parameters with their corresponding products are shown in Table 1.

From Product 1 to 4, as the concentration of FeCl $_2$  increases, the synthesized NPs get smaller. The TEM images (Figure 3a–c) with the same magnification as Figure 1a obviously show the monotonic size change. Size distributions were evaluated by randomly measuring 300 NPs in the images, also listed in Table 1. With the amount of FeCl $_2$ -4H $_2$ O increasing from 0.25 to 1.25 g, the size of the synthesized NPs decreases from 31.1 to 15.4 nm. This could be due to the fact that the concentration of Fe (II) ions strongly affects the nucleation and growth rate of Fe $_3$ O $_4$  particles. The higher initial precursor concentration led to smaller particles size due to the formation of a large number of seed nuclei, which provided high particle concentration and yielded smaller particles.  $^{40,46}$ 

Another important factor affecting the size of the synthesized  $Fe_3O_4$  NPs is the composition of the solvent. For Product 5, we replaced half the volume of water used for Product 1 preparation (6.375 mL) with ethanol, while keeping all other parameters unchanged. The resulting NPs have a significant size decrease (from 31.1 nm for Product 1 to 19.9 nm for Product 5), as can be seen from the TEM image and size distribution histogram in Figure 3d. Similar effects have been reported previously.  $^{47,48}$  The reason for this could be due to the fact that the formed  $Fe_3O_4$  NPs with considerable numbers of hydroxyl groups on the surface can absorb ethanol via hydrogen bond formation. Accordingly, there were more ethanol molecules attached on the NP surfaces, which inhibited the subsequent growth and aggregation of the particles, leading to the formation of smaller particles.

To further confirm the crystal structure and the size of the formed  $Fe_3O_4$  NPs under different conditions, XRD experiments were performed (Figure 4). The XRD patterns labeled from (a) to (e) correspond to Product 1 to 5, respectively. The lattice spacing calculated from the diffraction peaks observed at 30, 35.4, 37.2, 43, 53.4, 56.9, and 62.5 matched the [220], [311], [222], [400], [422], [511], and [440] planes of  $Fe_3O_4$  crystals, respectively. The XRD patterns are consistent with those reported in literature. $49^{-51}$  The comparison of pattern (e) with the other four patterns suggests that the use of water/ethanol mixture as solvent does not have any appreciable effect on the crystal structure of the NPs when compared to those NPs formed in pure water. To obtain the average size of the  $Fe_3O_4$  NPs, we performed fine scans on the major peak (plane [311]) of each product and calculated their sizes using Scherrer's equation. The results (Table 1) are in very good agreement with TEM data. It can be further concluded that the synthesized  $Fe_3O_4$  NPs are nearly single crystals.

## Magnetic properties of the Fe<sub>3</sub>O<sub>4</sub> NPs

The magnetic hysteresis loops of Fe<sub>3</sub>O<sub>4</sub> NPs at room temperature were obtained by a DC SQUID magnetometer (Figure 5). For the largest NPs (Product 1 with mean diameter of 31.1 nm), the specific saturation magnetization ( $\sigma_s$ ) is 97.4 emu/g, which is close to the bulk magnetite (92 emu/g).<sup>52</sup> The slightly higher  $\sigma_s$  of Product 1 could be due to the specific surface characteristics of the Fe<sub>3</sub>O<sub>4</sub> NPs prepared using our approach. In addition, the relative large size of Product 1 (31 nm) also contributes to the higher saturation magnetization. As the size of the Fe<sub>3</sub>O<sub>4</sub> NPs is reduced to 22.4, 16.7, and 15.4 nm,  $\sigma_s$  decreases to 81.2, 65.1 and 53.3

emu/g, respectively. This phenomenon was observed in many other magnetic NPs and could be explained by the existence of a magnetically inert layer on the surface of the particles. <sup>53</sup> Due to this surface effect,  $\sigma_s$  is contributed by an effective volume, which is a fraction of the nominal volume. As the particle gets smaller, the magnetic effective volume accounts for smaller proportion and the specific saturation magnetization decreases.

Figure 6 displays the profile of  $\sigma_s$  as a function of the inverse of the particle mean diameter. The data points were fitted linearly. A theoretical approach to quantitatively explain this linear relationship assumes that each nanocrystal consists of two parts: the nonmagnetic outer layer with thickness t and magnetic normal core with the same property as bulk material. By keeping the first order in t, the specific saturation magnetization is found to be proportional to the inverse of diameter.

$$\sigma_s(d) = \left(1 - \frac{6t}{d}\right)\sigma_s(\infty) \tag{4}$$

The nonmagnetic layer on the surface of the  $Fe_3O_4$  NPs can be calculated, and is found to be about 1.4 nm.

As can be seen from Figure 5b, in the particle size range of our synthesized products (from 31.1 to 15.4 nm) ferromagnetism was observed. But as the mean size decreases, the coercivity (H<sub>c</sub>) also decreases to values smaller than the reported for ferromagnetic bulk material. This suggests a gradual transition from ferromagnetism to superparamagnetism as a function of the size of the magnetic NPs. This transition meets the requirements for using these NPs as contrast agent in the SQUID-MRX measurement. Due to the millisecond time delay between the biasing field turning off and measurements starting, NPs that are far in the region of superparamagnetism decay too rapid to be detected. On the other hand, large particles can not generate detectable decay signal during the measurement time course and will also be ignored. So only the NPs on the magnetic properties transition region with the appropriate relaxivity rate provide signal contribution, and thus preferred by the MRX technique.

#### **SQUID-MRX** results

Figure 7 shows a typical relaxation curve recorded by the SQUID-MRX system with the theoretical fitting for 200  $\mu$ g NPs of Product 4. The "no sample" curve in Figure 7 was acquired in the absence of the Fe<sub>3</sub>O<sub>4</sub> NPs after the background was subtracted. By applying Equation (3) to fit the experimental curve in the presence of NPs, the best-fit parameters B' and B<sub>0</sub> can be determined to be 87.9 and 20.5 pT, respectively. The value of B' can be ignored because it contains no information about the sample. B<sub>0</sub> depends on a number of parameters, including the biasing field strength, signal recording time, distance from the sample to SQUID detector, mass of the NPs, etc. However, as long as the SQUID detection parameters do not change, B<sub>0</sub> is only affected by the mass of NPs. This relationship can be well fitted with a linear equation, shown in Figure 8.

As discussed above, when the average size of the iron oxide magnetic NPs is decreased from 31.1 to 15.4 nm, the magnetic behavior changes from ferromagnetic to superparamagnetic. This transition affects the particles' relaxation time constant, which in turn increases the MRX signal intensity. To test this, similar amounts of iron oxide NPs (200  $\mu$ g) from Products 1 to 4 were prepared and measured by SQUID-MRX. The decay amplitudes (i.e. B<sub>0</sub>) for different products were found to increase as the particle size decreases (Figure 9), with a signal enhancement of three folds as the average size changing from 31.1 to 15.4nm. The size dependence of MRX signal can be understood by considering the Nèel relaxation's relation to

particle size. According to equation (2), larger NPs have longer magnetic decay time. When the decay time is long enough that no obvious decay can be observed during the MRX measurement time interval (in our case, 1 s), such particles have no contribution to the measurement. As the average size decreases, larger portion of NPs will have the decay time less than or equal to 1 s, thus increasing the MRX signal. And this behavior can be supported by the magnetic property transition from ferromagnetism to superparamagnetism (Figure 5).

#### Conclusion

In summary, we report a facile route to hydrothermally synthesizing iron oxide NPs with controllable size and tunable magnetic properties. The diameter ranges from 15 to 30 nm by changing the concentration of the reactants or the reaction solvent composition. The resultant Fe<sub>3</sub>O<sub>4</sub> NPs are single crystals and have high purity. Their magnetic property exhibits a transition from ferromagnetic to superparamagnetic behavior as the particle's diameter decreases. Within the diameter range of the synthesized NPs, we show that the NPs with a smaller size has higher signal in SQUID-MRX measurement. With the recent advances in the development of shell-crosslinked iron oxide nanoparticles for in vivo magnetic resonance (MR) imaging of tumors, <sup>12</sup> it is expected that the synthesized iron oxide NPs should be able to be modified and conjugated with specific targeting ligands for future MR and SQUID imaging of tumors. We are currently actively pursuing this area of research.

# **Acknowledgments**

This project has been funded in whole or in part by the National Institutes of Health (NIH) (under the contract # NIH 1 RO1 EB002657, NOI-CO-97111, and NIH 1 RO1 CA119409) and the Michigan Economic Development Corporation-Life Sciences Corridor Fund (under award GR-472). The XPS instrument used in this work was funded by NSF through the Grant DMR-0420785. X Shi thanks the support from the Program for Professor of Special Appointment (Eastern Scholar) at Shanghai Institutions of Higher Learning and the National Basic Research Program of China (973 Program, 2007CB936000). We thank Roger A. Pinto for using the Autoclave in his lab, Sasha Meshinchi for his assistance with the TEM experiments, and Lindsay Shuller for her help with the XRD experiments.

#### References and Notes

- 1. Rosi NL, Mirkin CA. Chem Rev 2005;105:1547. [PubMed: 15826019]
- 2. Daniel MC, Astruc D. Chem Rev 2004;104:293. [PubMed: 14719978]
- 3. Moghimi SM, Hunter AC, Murray JC. FASEB J 2005;19:311. [PubMed: 15746175]
- 4. Parak WJ, Gerion D, Pellegrino T, Zanchet D, Micheel C, Williams SC, Boudreau R, Le Gros MA, Larabell CA, Alivisatos AP. Nanotechnology 2003;14:R15.
- 5. Gupta AK, Gupta M. Biomaterials 2005;26:3995. [PubMed: 15626447]
- Samanta B, Yan H, Fischer NO, Shi J, Jerry DJ, Rotello VM. J Mater Chem 2008;18:1204. [PubMed: 19122852]
- Sun C, Fang C, Stephen Z, Veiseh O, Hansen S, Lee D, Ellenbogen RG, Olson J, Zhang MQ. Nanomedicine 2008;3:495. [PubMed: 18694312]
- 8. Kohler N, Sun C, Wang J, Zhang MQ. Langmuir 2005;21:8858. [PubMed: 16142971]
- 9. Mornet S, Vasseur S, Grasset F, Duguet E. J Mater Chem 2004;14:2161.
- 10. Morawski AM, Lanza GA, Wickline SA. Curr Opin Biotechnol 2005;16:89. [PubMed: 15722020]
- 11. Gao SY, Shi YG, Zhang SX, Jiang K, Yang SX, Li ZD, Takayama-Muromachi E. J Phys Chem C 2008;112:10398.
- 12. Shi XY, Wang SH, Swanson SD, Ge S, Cao ZY, Van Antwerp M, Landmark KJ, Baker JR. Adv Mater 2008;20:1671.
- 13. Fried T, Shemer G, Markovich G. Adv Mater 2001;13:1158.
- 14. Kang YS, Risbud S, Rabolt JF, Stroeve P. Chem Mater 1996;8:2209.
- 15. Shi XY, Thomas TP, Myc LA, Kotlyar A, Baker JR. Phys Chem Chem Phys 2007;9:5712. [PubMed: 17960261]

- 16. Tang J, Myers M, Bosnick KA, Brus LE. J Phys Chem B 2003;107:7501.
- 17. Hyeon T, Lee SS, Park J, Chung Y, Bin Na H. J Am Chem Soc 2001;123:12798. [PubMed: 11749537]
- 18. Sun SH, Zeng H. J Am Chem Soc 2002;124:8204. [PubMed: 12105897]
- 19. Landmark KJ, DiMaggio S, Ward J, Kelly C, Vogt S, Hong S, Kotlyar A, Myc A, Thomas TP, Penner-Hahn JE, Baker JR, Holl MMB, Orr BG. ACS Nano 2008;2:773. [PubMed: 19206610]
- 20. Yu WW, Chang E, Sayes CM, Drezek R, Colvin VL. Nanotechnology 2006;17:4483.
- 21. Cohen D. Science 1973;180:745. [PubMed: 4702572]
- 22. Berry CC, Charles S, Wells S, Dalby MJ, Curtis ASG. Int J Pharm 2004;269:211. [PubMed: 14698593]
- 23. Moore A, Josephson L, Bhorade RM, Basilion JP, Weissleder R. Radiology 2001;221:244. [PubMed: 11568347]
- 24. Veiseh O, Sun C, Gunn J, Kohler N, Gabikian P, Lee D, Bhattarai N, Ellenbogen R, Sze R, Hallahan A, Olson J, Zhang MQ. Nano Lett 2005;5:1003. [PubMed: 15943433]
- 25. Wang SH, Shi XY, Van Antwerp M, Cao ZY, Swanson SD, Bi XD, Baker JR. Adv Funct Mater 2007;17:3043.
- 26. Enpuku K, Kuroda D, Ohba A, Yang TQ, Yoshinaga K, Nakahara T, Kuma H, Hamasaki N. Jpn J Appl Phys 2003;42:L1436.
- 27. Kotitz R, Matz H, Trahms L, Koch H, Weitschies W, Rheinlander T, Semmler W, Bunte T. IEEE Trans Appl Supercond 1997;7:3678.
- 28. Enpuku K, Minotani T, Gima T, Kuroki Y, Itoh Y, Yamashita M, Katakura Y, Kuhara S. Jpn J Appl Phys 1999;38:L1102.
- 29. Enpuku K, Minotani T, Hotta M, Nakahodo A. IEEE Trans Appl Supercond 2001;11:661.
- 30. Tanaka S, Ota H, Kondo Y, Tamaki Y, Kobayashi S, Noguchi S. IEEE Trans Appl Supercond 2003;13:377.
- 31. Chemla YR, Crossman HL, Poon Y, McDermott R, Stevens R, Alper MD, Clarke J. Proc Natl Acad Sci U S A 2000;97:14268. [PubMed: 11121032]
- 32. Grossman HL, Myers WR, Vreeland VJ, Bruehl R, Alper MD, Bertozzi CR, Clarke J. Proc Natl Acad Sci U S A 2004;101:129. [PubMed: 14688406]
- 33. Haller A, Matz H, Hartwig S, Kerberger T, Atzpadin H, Trahms L. IEEE Trans Appl Supercond 2001;11:1371.
- 34. Lange J, Kotitz R, Haller A, Trahms L, Semmler W, Weitschies W. J Magn Magn Mater 2002;252:381.
- 35. Lee S, Myers WR, Grossman HL, Cho HM, Chemla YR, Clarke J. Appl Phys Lett 2002;81:3094.
- 36. Flynn ER, Bryant HC. Phys Med Biol 2005;50:1273. [PubMed: 15798322]
- 37. Fannin PC, Charles SW. J Phys D-Appl Phys 1991;24:76.
- 38. Fannin PC, Charles SW. J Phys D-Appl Phys 1994;27:185.
- 39. Chantrell RW, Hoon SR, Tanner BK. J Magn Magn Mater 1983;38:133.
- 40. Hui C, Shen CM, Yang TZ, Bao LH, Tian JF, Ding H, Li C, Gao HJ. J Phys Chem C 2008;112:11336.
- 41. Vereda F, de Vicente J, Morales MDP, Rull F, Hidalgo-Alvarez R. J Phys Chem C 2008;112:5843.
- 42. Cornell, RM.; Schwertmann, U. The Iron Oxides. 2. VCH; Weinheim: 2003.
- 43. McClune, WF. Powder diffraction File Alphabetical Index Inorganic Phase. JCPDS; Swarthmore: 1980.
- 44. Moudler, JF.; Stickle, WF.; Sobol, PE.; Bonben, KD. Handbook of X-ray Photoelectron Spectroscopy. Perkin-Elmer; Eden Prairie, MN: 1992.
- 45. Zhang DE, Zhang XJ, Ni XM, Song JM, Zheng HG. Cryst Growth Des 2007;7:2117.
- 46. Shevchenko E, Talapin D, Kornowski AL, Rogach A, Kormowski A, Haase M, Weller H. J Am Chem Soc 2002;124:11480. [PubMed: 12236762]
- 47. Dong YM, He K, Yin L, Zhang AM. Nanotechnology 2007;18:435602/1.
- 48. Liang X, Wang X, Zhuang J, Chen YT, Wang DS, Li YD. Adv Funct Mater 2006;16:1805.
- 49. Harris LA, Goff JD, Carmichael AY, Riffle JS, Harburn JJ, St Pierre TG, Saunders M. Chem Mater 2003;15:1367.

50. Maoz R, Frydman E, Cohen SR, Sagiv J. Adv Mater 2000;12:424.

- 51. Sun SH, Zeng H, Robinson DB, Raoux S, Rice PM, Wang SX, Li GX. J Am Chem Soc 2004;126:273. [PubMed: 14709092]
- 52. Chikazumi, S. Physics of Magnetism. Wiley; New York: 1964.
- 53. Yang H, Shen LC, Zhao LJ, Song LZ, Zhao JZ, Wang ZC, Wang L, Zhang D. Mater Lett 2003;57:2455.

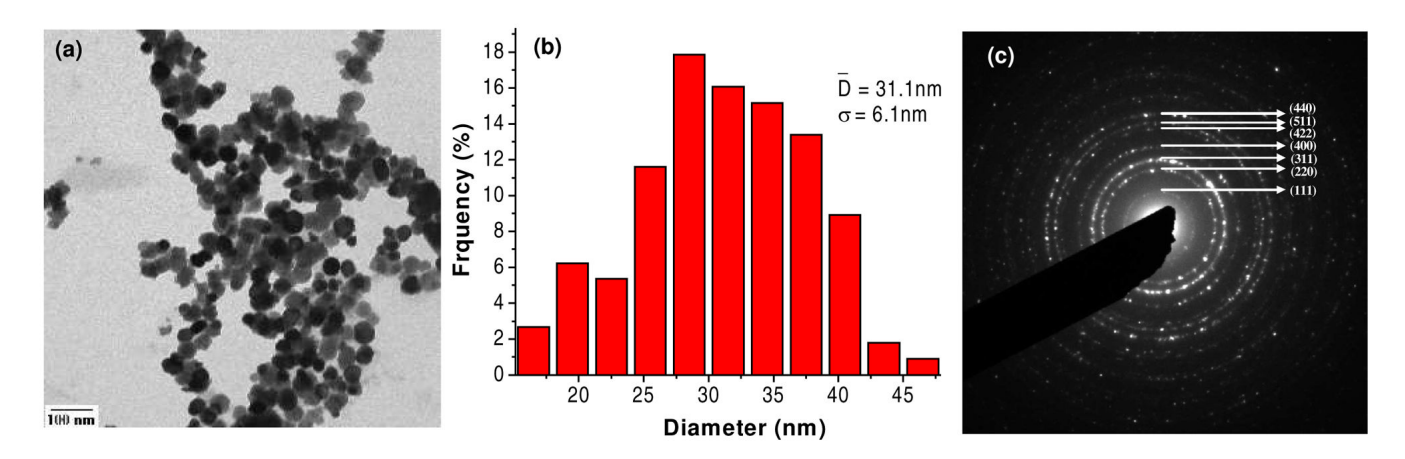


**Figure 1.**A typical TEM image (a), size distribution histogram (b), and selected area electron diffraction (SEAD) pattern (c) of Fe<sub>3</sub>O<sub>4</sub> NPs (Product 1 listed in Table 1).

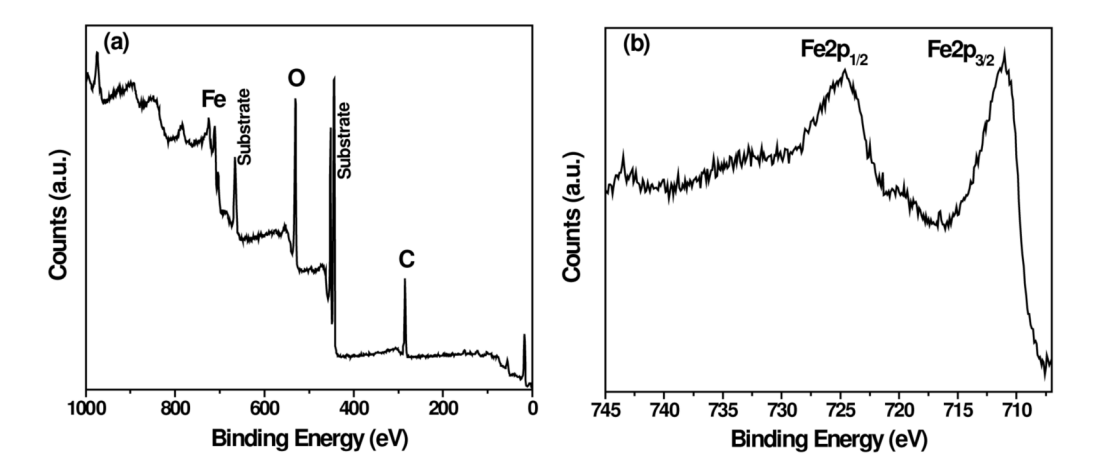


Figure 2. XPS survey of the as-synthesized  $Fe_3O_4$  NPs (a) and Fe2p core-level spectrum (b) of the same NPs (Product 1 listed in Table 1).

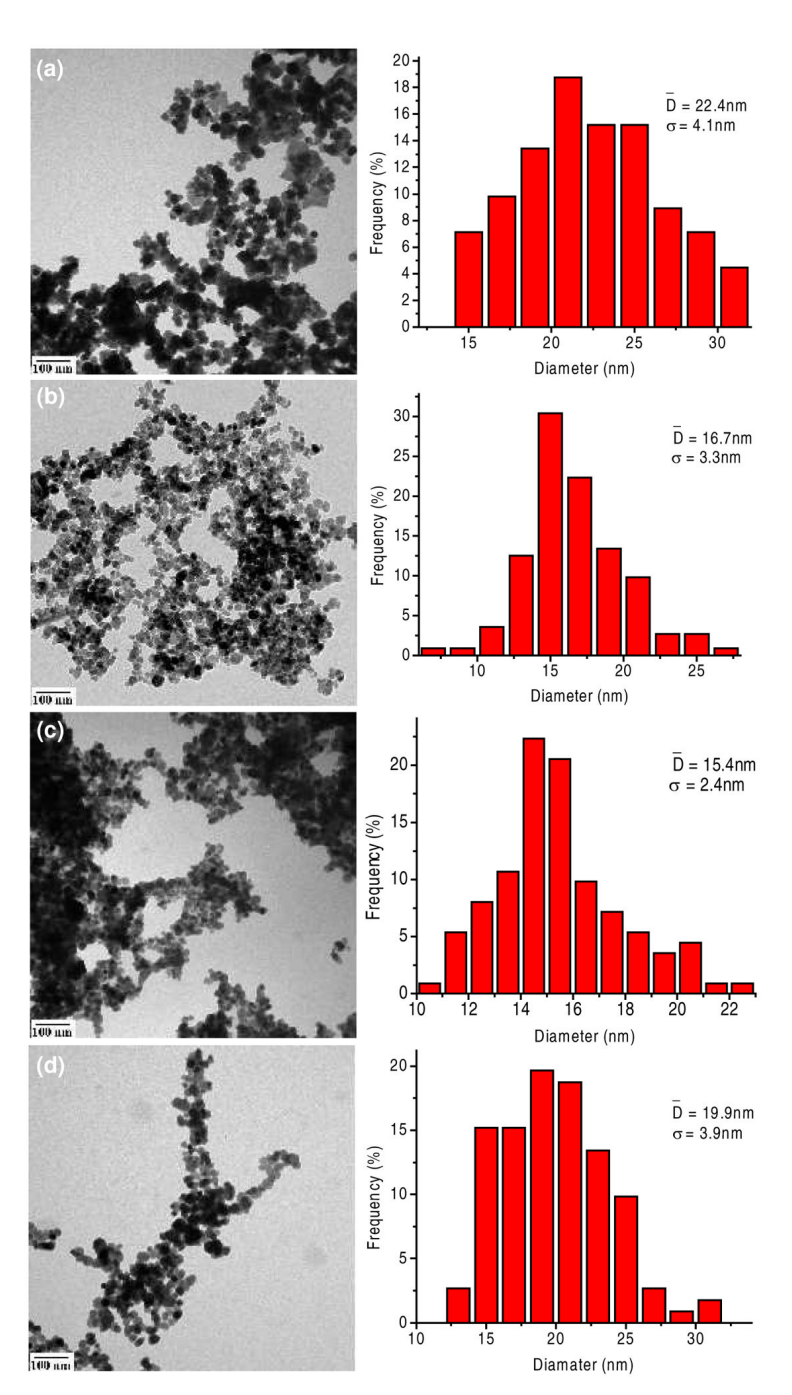
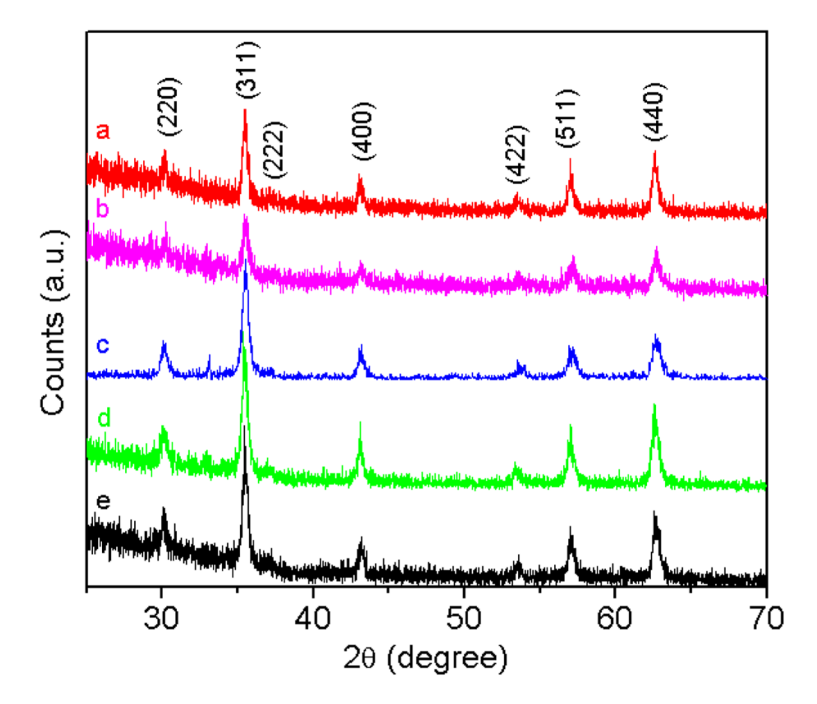
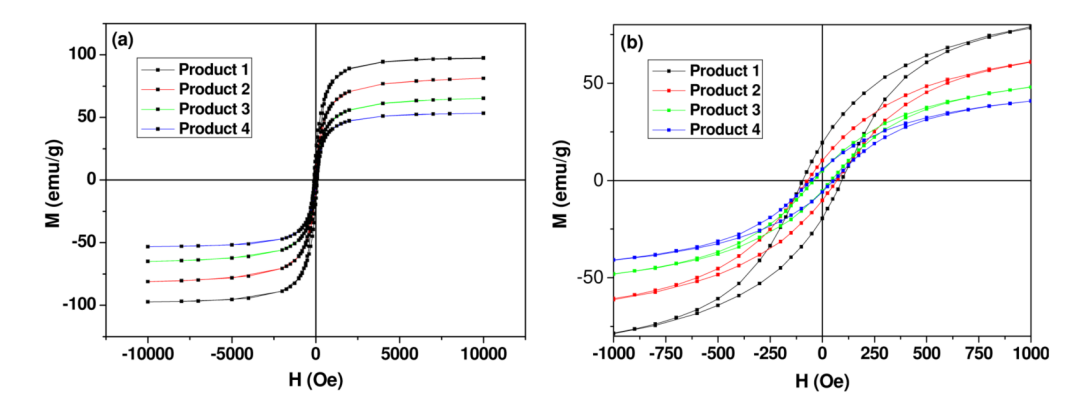


Figure 3. TEM images of  $Fe_3O_4$  NPs as the concentration of  $FeCl_2$  increasing and the corresponding statistical histograms. Mean diameters are (a) 22.4nm (b) 16.7nm (c) 15.4nm. Same condition as the NPs in Figure 1 except that ethanol and water mixture was used as solvent (d) mean diameter 19.9nm.



**Figure 4.**XRD patterns of (a) Product 1 (29.7 nm), (b) Product 2 (22.5 nm), (c) Product 3 (17.3 nm), (d) Product 4 (16.0 nm), and (e) Product 5 (20.3 nm) (see Table 1). The diameter of each product is calculated based on Scherrer's equation.



**Figure 5.**SQUID magnetometry measurement of room-temperature magnetic hysteresis of NP Products 1–4: (a) full hysteresis loops, and (b) hysteresis at low field.

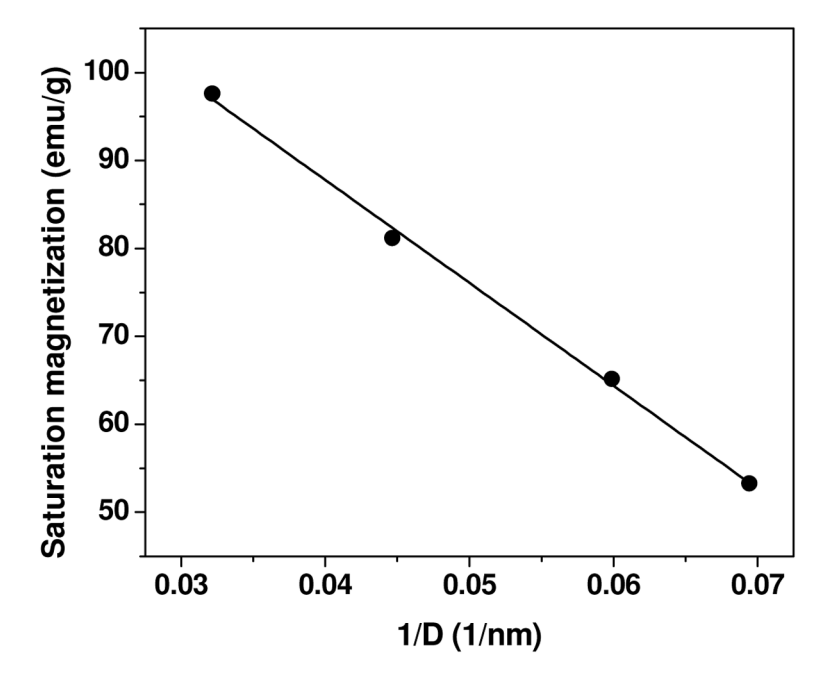


Figure 6. The saturation magnetization  $(\sigma_s)$  decreases as the diameter of the Fe<sub>3</sub>O<sub>4</sub> NPs increases due to the nonmagnetic surface effect.

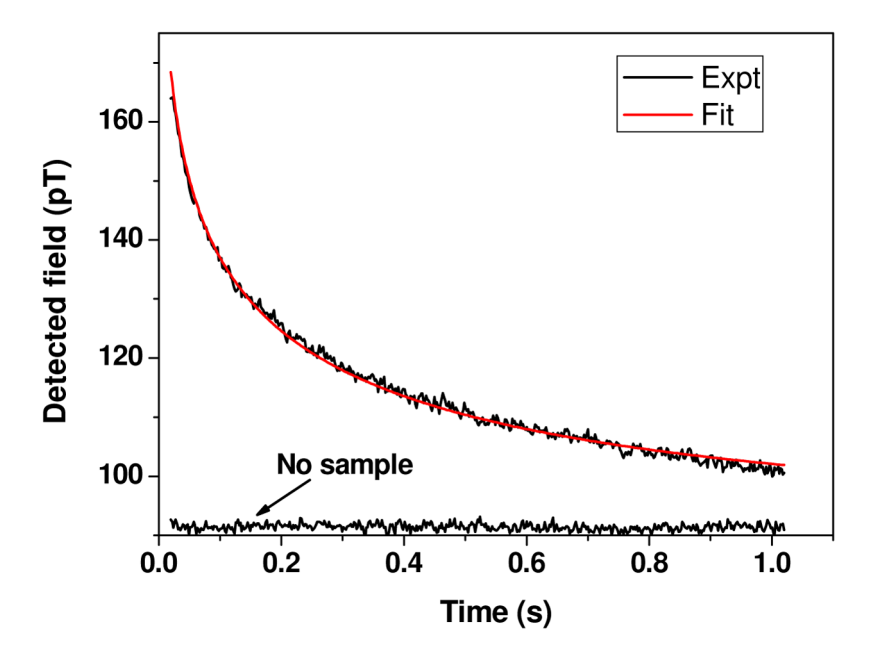


Figure 7. Typical SQUID magnetorelaxometry curve with theoretical fitting  $B(t) = B_0 ln(1+1/t) + B'$ , where  $B_0 = 2.05 \times 10^{-11} T$  and  $B' = 8.79 \times 10^{-11} T$ . The factor  $B_0$  is proportional to the amount of NPs as shown in Figure 8.

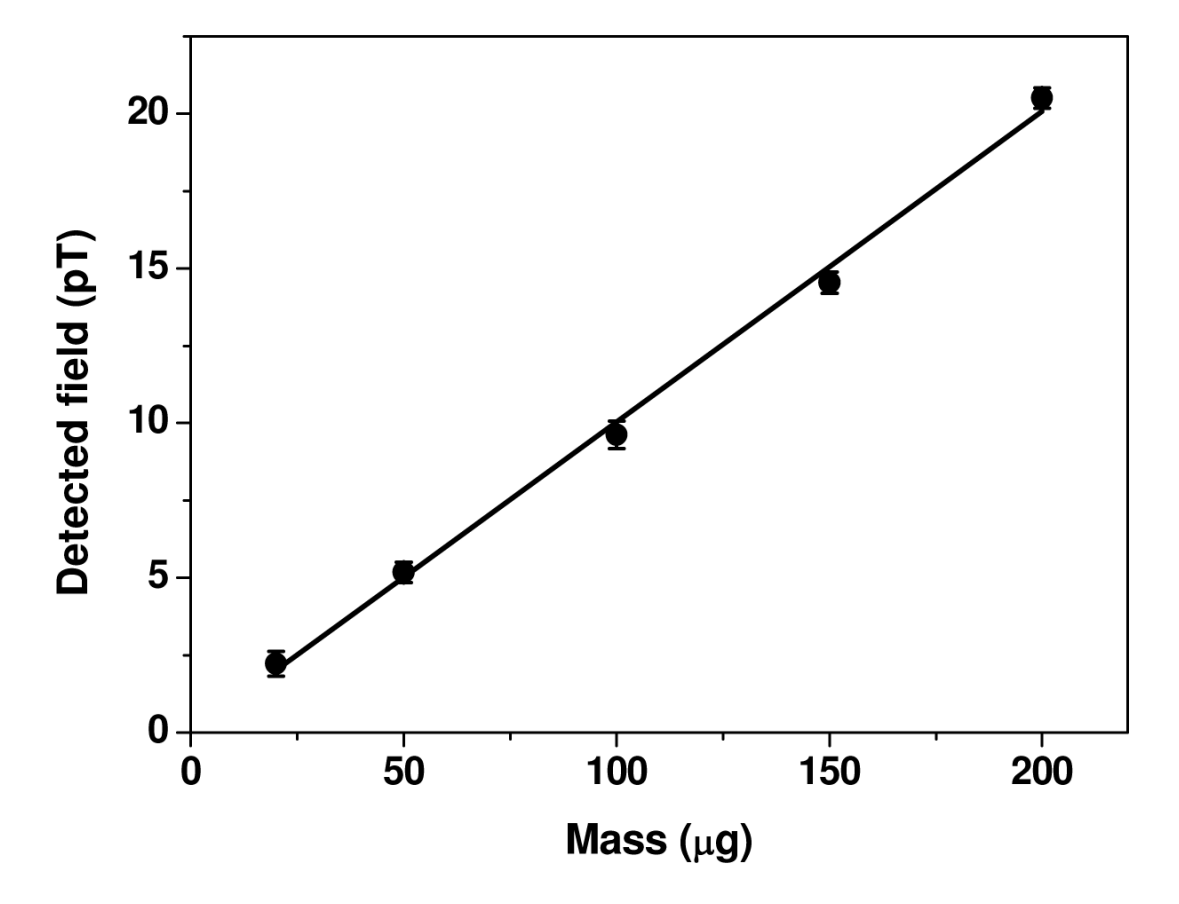


Figure 8. A calibration curve shows a linear relationship between the detected magnetic field ( $B_0$  from equation 3) and iron mass of  $Fe_3O_4$  NPs. All data points were obtained by averaging over 50 measurements.

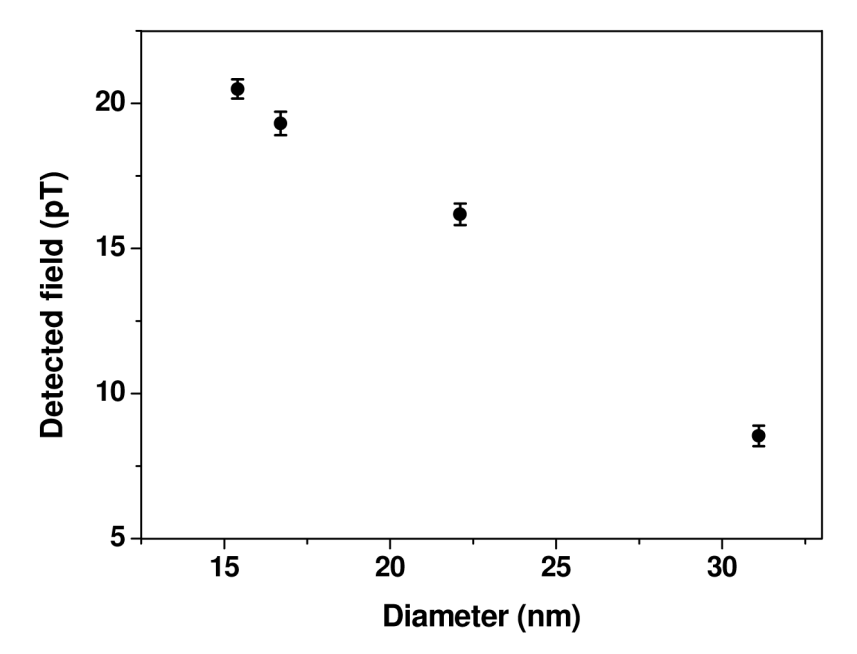


Figure 9. Constant mass of Fe $_3$ O $_4$  NPs (200  $\mu$ g) from each product (Products 1–4) shows that smaller particles have the larger magnetic field signal.

Table 1

Ge et al.

 $\mathrm{Fe_3O_4}\,\mathrm{NPs}$  with tunable sizes synthesized under different reaction conditions.

		So	Solvent				
Pruduct	Pruduct FeCl <sub>2</sub> ·4H <sub>2</sub> O (g)	$ m H_2O~(mL)$	Ethanol (mL)	$NH_3 \cdot H_2O\left(mL\right)$	${ m NH_3 \cdot H_2 O}$ (mL) Total volume (mL) Diameter $^a$ (nm) Diameter $^b$ (nm)	Diameter $a$ (nm)	Diameter $^{b}$ (nm)
1	0.25	12.75	0	1.25	14	$31.1 \pm 6.1$	29.7
2	0.5	11.5	0	2.5	14	$22.4 \pm 4.1$	22.5
ю	1	6	0	5	14	$16.7 \pm 3.3$	17.3
4	1.25	7.75	0	6.25	14	$15.4 \pm 2.4$	16.0
5	0.25	6.375	6.375	1.25	14	$19.9 \pm 3.9$	20.3

 $^{a}$ Measured by TEM.

 $^{b}$  Measured by XRD.

Page 19